Electrochimica Acta 401 (2022) 139512

Contents lists available at ScienceDirect

Electrochimica Acta

journal homepage: www.elsevier.com/locate/electacta

A peridynamic model for crevice corrosion damage

Siavash Jafarzadeh [a], Jiangming Zhao [a], Mahmoud Shakouri [b], Florin Bobaru [a,*]

[a] Department of Mechanical and Materials Engineering, University of Nebraska-Lincoln, Lincoln, NE 68588-0526, United States
[b] Department of Construction Management, Colorado State University, Fort Collins, Co 80523, United States

ARTICLE INFO

Article history:
Received 31 August 2021
Revised 26 October 2021
Accepted 27 October 2021
Available online 31 October 2021

Keywords:
Crevice corrosion
Peridynamics
Corrosion
Modeling
Nonlocal mass transfer
Nickel alloy

ABSTRACT

A new peridynamic (PD) model for crevice corrosion damage is introduced and cross-validated with experimental results from the literature. Electrochemical mechanisms are reduced to a simple metal-ion concentration-dependent corrosion rate. Computations over domains with extreme aspect ratios like those seen in crevices are efficiently performed by modifying the PD formulation to accommodate arbitrary-shape horizons. The model is validated against experimental results on bolted washers. Simulations predict both the location and the depth of deep corrosion trenches that form at a distance from the crevice mouth. Far-field boundary conditions are used to autonomously reproduce the experimentally observed progression of crevice corrosion. The PD model results also show that the two factors considered here (diffusion-driven transport of dissolved metal ions, and dissolution being dependent on their concentration) are sufficient to predict the evolution of crevice corrosion.

1. Introduction

Crevice corrosion is a type of localized corrosion that occurs in locations where the metallic surface is exposed to a confined, stagnant electrolyte in a "crevice," while the rest of the metallic surface is in contact with the bulk electrolyte [1]. Crevice corrosion of passive metals occurs above critical potentials and temperatures, in the presence of a depassivating agent (mostly chloride) while in the case of non-passive metals crevice/under-deposit corrosion occurs in non-specific environments as they are actively corroding. In both cases however, restricted flow in the crevice slows down the transport of chemical species and leads to local acidification (pH drop), triggering a self-accelerating anodic dissolution of the metal surface in the crevice [1]. The initiation stage of crevice corrosion is slow, as it can span months/years. In contrast, the propagation phase may happen significantly faster due to the highly corrosive environment formed in the crevice ([2], page 272). Crevice corrosion damage is considered a significant problem in many industries. Joints, fasteners, and most types of contacts in ships, aircrafts, infrastructures, or any other structures in offshore and marine environments, are highly susceptible to crevice corrosion attack [3,4]. For example, in bridges' tendons, crevice corrosion occurs between strands and the grout surrounding them and even between twisted wires in a strand, and may contribute to catastrophic failure of bridges [5].

Computational models for corrosion damage phenomena, if predictive, are of significant interest since they provide a tool to virtually investigate the potential damage caused by environmental factors [6]. Computational models output chemical speciation, the evolution of various electrolyte properties such as pH, conductivity, and, more importantly, potential and current density profiles, which ultimately can determine the corrosion rate. Models for crevice corrosion are of two classes: 1) *the first class uses a stationary domain*, where the governing equations (usually mass transport and electrostatics) are solved within a fixed time-invariant domain (inside the crevice only) [7–19]. The second class of crevice corrosion models considers an *evolving geometry*, where the anodic dissolution changes the shape of the crevice in time as corrosion progresses [20–24]. The first class of models is, obviously, computationally more efficient. However, such models have obvious limitations because, at best, they can only provide rough estimates of the corrosion profile based on the computed current densities over the original crevice domain (see for example [25,26]). Since changes in the crevice geometry influence the transport phenomenon and the electric potential distribution on the anodic surface, the second class is closer to reality, and they can provide a corrosion damage front profile. This profile is important because, under mechanical loadings, cracks can initiate from the deep trenches carved by crevice corrosion attack [5].

Traditionally, corrosion problems with evolving domains have been described by Partial Differential Equations (PDEs)-based models. Some of such models have regarded corrosion as a moving boundary problem. For example, the Finite Element Method has been used to solve the PDEs in the domain configuration at each

* Corresponding author.
E-mail address: fbobaru2@unl.edu (F. Bobaru).

https://doi.org/10.1016/j.electacta.2021.139512
0013-4686/

time step and the level set [22] or Arbitrary Lagrangian-Eulerian (ALE) [21] methods are used to update the domain boundary, leading to a new domain configuration for the next time step. Models with moving boundaries face serious challenges in their discretization as they need to change the domain and meshes at each time step. The limitations of these models are further discussed in [6,27]. Some other PDE-based models consider corrosion propagation as a moving interface problem in a domain consisting of both the liquid phase (electrolyte) and a solid phase (metal) (see, e.g., [20]). However, because these models need to determine and apply their boundary conditions along the unknown moving interface (that is supposed to be the solution to the problem and requires to be explicitly tracked in these methods), accuracy suffers since extra assumptions have to be made and these often push the results away from what is observed experimentally.

More recently, a new class of models has emerged that solve the governing equations defined over a two-phase, electrolyte-solid domain, and predict the evolution of the corrosion front caused by anodic dissolution more efficiently This approach eliminates the need to explicitly track the corrosion front, simplifies numerical complexity, and improves a model's applicability to more complex situations. An example of such models is Cellular Automata (CA) [28,29]. However, given their discrete nature and their use of heuristic rules for "cell" transformation, they are difficult to calibrate and less applicable for quantitative predictions [6]. While CAs may offer results that replicate certain qualitative aspects of an observed phenomenon, validations against experimental results are almost non-existent in the published literature.

Peridynamic (PD) models of corrosion [30–33] are another example of models that does not require tracking the moving boundary explicitly. PD is a nonlocal approach that replaces spatial derivatives with integrals in its formulations. This change allows PD models to naturally capture autonomous emergence and evolution of discontinuities, moving boundaries, and critical features in modeling corrosion damage. PD models have been shown to be remarkably accurate in modeling fracture [34,35], corrosion-induced fracture [36], and stress corrosion cracking [37,38].

A third example of corrosion models that do not require the explicit tracking of the corrosion front is given by phase-field (PF) models. PF corrosion models [23,39] are PDE-based models of corrosion that approximate the material discontinuity at the corrosion front with a smooth transition function over a small length scale, so that spatial derivatives can exist. PF models have shown promise in some corrosion problems, but challenges persist. For example, unrealistically thick cracks/damages develop when simulating corrosion-induced fracture and damage [40,41]. They also tend to be very demanding computationally since they require to solve systems of PDEs.

To date, no crevice corrosion model has been quantitatively cross-validated with published experimental results in terms of evolution of damage. In this study, we introduce a simple and predictive peridynamic model for simulating crevice corrosion damage. The model is based on reducing a complex phenomenon to essentially a dependence of corrosion rate on the local metal ion concentration. While crevices are often 3D interconnected channels, experiments like the ones in [42] provide results along 2D sections that will allow us to compare and validate our general PD model using 2D simulations. Most crevices that naturally form between mating surfaces have extreme aspect ratios with effectively micrometer-sized gaps and centimeter-sized lengths, like in fasteners. In order to achieve computational efficiency in problems with high aspect ratio geometries, a modified version of the peridynamics formulation (with non-circular/non-spherical horizon regions) is presented, allowing domain discretizations that mimic the given geometry extreme aspect ratio. The model is validated against published experimental images on the progression of crevice corrosion damage in bolted washers.

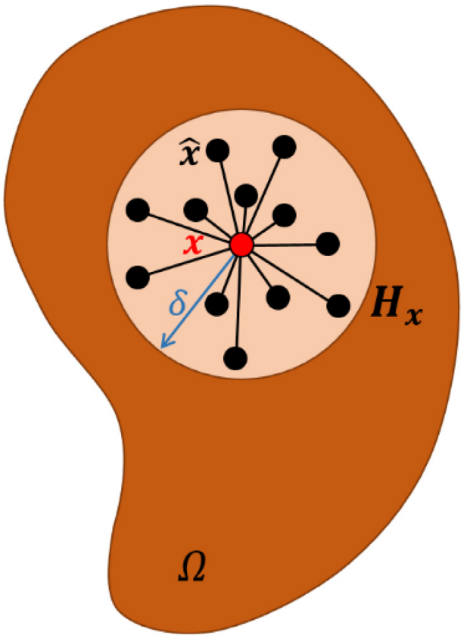

Fig 1. Schematic of a peridynamic body Ω, and the nonlocal interactions between a generic material point and its family (from [33]).

2. Peridynamic corrosion models

In this section, we briefly review the basics of peridynamic (PD) theory, the general formulation of PD corrosion models, and the employed discretization method.

2.1. Peridynamics

Peridynamics theory is a nonlocal extension of continuum mechanics [43,44]. In this theory, each material point interacts with other material points that are located within its finite size neighborhood. For a point with the position vector $\boldsymbol{x}$, the finite size neighborhood (H_x), which is usually taken to be a sphere in 3D (or a disk in 2D, a line segment in 1D) centered at $\boldsymbol{x}$ with the radius δ called horizon size. In Section 4 we present a formulation for horizon sizes of arbitrary shapes, including extremely elongated ones, useful in treating problem with extreme aspect ratios. Other points inside H_x are called the "family" of $\boldsymbol{x}$ and are denoted by the position vector $\hat{\boldsymbol{x}}$. Fig. 1, schematically shows a PD body, a generic point $\boldsymbol{x}$, its horizon, and family nodes.

The term PD *bond* refers to objects that carry the nonlocal interactions between two family points. There are different types of bonds, depending on the type of interaction. For example, in a mechanical problem, PD *mechanical bonds* transmit force densities between points, while for diffusion problems, PD *diffusion bonds* carry heat/mass between family points.

2.2. Peridynamics modeling of corrosion damage

The PD corrosion damage model was originally introduced in [30] and later modified in [33]. In this part, we briefly layout the PD corrosion damage formulation based on the modified version in [33].

2.2.1. Formulation of peridynamic corrosion damage

PD corrosion model is based on a damage-dependent nonlocal diffusion equation that governs the mass transport in a two-

phase domain consisting of both metal (solid) and electrolyte (liquid) phases. In this model, the "metal-ion concentration" field C, is used as a single "umbrella" parameter, intended to represent all of the dissolved cations from the metal substrate, and thus the total mass-loss from the solid. The PD model can be extended to a more sophisticated version in which each chemical species of interest is represented separately by a different parameter. However, as will be shown in the results section, the presented minimalistic approach seems to be sufficient to correctly predict the major characteristics experimentally observed for crevice corrosion.

The governing equations are as follows:

$$\frac{\partial C(\boldsymbol{x},t)}{\partial t} = \int_{H_x} k\left(\boldsymbol{x},\hat{\boldsymbol{x}},t\right)\frac{C\left(\hat{\boldsymbol{x}},t\right)-C(\boldsymbol{x},t)}{\left|\hat{\boldsymbol{x}}-\boldsymbol{x}\right|^2}\mathrm{d}V_{\hat{x}} \tag{1}$$

$$k\left(\boldsymbol{x},\hat{\boldsymbol{x}},t\right) = \begin{cases} k_{\mathrm{diff}}(D,\delta) & \text{, if } d(\boldsymbol{x})=1 \text{ and } d\left(\hat{\boldsymbol{x}}\right)=1 \\ 0 & \text{, if } d(\boldsymbol{x})<1 \text{ and } d\left(\hat{\boldsymbol{x}}\right)<1 \\ k_{\mathrm{diss}}(i) & \text{, if } d(\boldsymbol{x})=1 \text{ xor } d\left(\hat{\boldsymbol{x}}\right)=1 \end{cases} \tag{2}$$

$$d(\boldsymbol{x},t) = 1 - \frac{\int_{H_x}\mu\left(\boldsymbol{x},\hat{\boldsymbol{x}},t\right)\mathrm{d}V_{\hat{x}}}{\int_{H_x}\mathrm{d}V_{\hat{x}}} \tag{3}$$

$$\mu\left(\boldsymbol{x},\hat{\boldsymbol{x}},t\right) = \begin{cases} 1 & \text{, if there is an intact mechanical bond between } \boldsymbol{x} \text{ and } \hat{\boldsymbol{x}} \text{ at time } t \\ 0 & \text{, if there is no mechanical bond between } \boldsymbol{x} \text{ and } \hat{\boldsymbol{x}} \text{ at time } t \end{cases} \tag{4}$$

$$d_c(\boldsymbol{x},t) = \begin{cases} 1, & C(\boldsymbol{x},t) \le C_{\mathrm{sat}} \\ \frac{C_{\mathrm{solid}}-C(\boldsymbol{x},t)}{C_{\mathrm{solid}}-C_{\mathrm{sat}}}, & C_{\mathrm{sat}} < C(\boldsymbol{x},t) \le C_{\mathrm{solid}} \end{cases} \tag{5}$$

In Eq. (1), $C(\boldsymbol{x},t)$ denotes the concentration of the dissolving species (here metal atoms/ions) at point $\boldsymbol{x}$ and time t. For the solid state, C is considered to be the molar concentration (moles per unit volume) of the alloy as a whole, regarded as the averaged molar mass (moles per unit mass) of the constituents with respect to their weight percentage, divided by the alloy's density (mass per unit volume). Once the metal is dissolved, it is assumed that the alloy's constituent elements become cations, and therefore, values of C in the liquid represent the molar concentration of the dissolved cations in an average sense.

The integrand is the *mass flow density* which is the molar amount that a unit volume at point $\boldsymbol{x}$ receives from the unit volume at a family point $\hat{\boldsymbol{x}}$ in one second. $\mathrm{d}V_{\hat{x}}$ is the differential volume at point $\hat{\boldsymbol{x}}$, and $k(\boldsymbol{x},\hat{\boldsymbol{x}},t)$ is a constant that is determined from Eq. (2), based on the phases of the points $\boldsymbol{x}$ and $\hat{\boldsymbol{x}}$ (solid or liquid) at time t. In this model, phases are represented by their damage index: the scalar $d(\boldsymbol{x},t) \in [0,1]$. If $d(\boldsymbol{x},t)=1$ at a point $\boldsymbol{x}$ and time t, then $\boldsymbol{x}$ is in the liquid phase, and if $0 \le d(\boldsymbol{x},t) < 1$, then $\boldsymbol{x}$ is the solid phase. The *bond damage* quantity $\mu(\boldsymbol{x},\hat{\boldsymbol{x}},t)$ defined by Eq. (4) is binary, and only takes values 0 or 1. The nodal damage index $d(\boldsymbol{x},t)$ (defined in Eq. (3)) is essentially the ratio of broken bonds to the total number of bonds at a node, and therefore, can vary between zero and one. Eq. (3) is simply the continuum version of the bonds ratio just mentioned.

According to Eq. (2), for the liquid-liquid bonds (bonds connecting two liquid points) $k = k_{\mathrm{diff}}$. k_{diff} is called the micro-diffusivity and is a function of the classical diffusivity of the electrolyte (D) and the horizon size (δ):

$$k_{\mathrm{diff}}(D,\delta) = \begin{cases} \frac{D}{\delta} & \text{, for 1D} \\ \frac{4D}{\pi\delta^2} & \text{, for 2D} \\ \frac{9D}{\pi\delta^3} & \text{, for 3D} \end{cases} \tag{6}$$

This parameter allows modeling of diffusion of metal ions in the electrolyte. Since C represents all of the cations dissolved from the substrate, the classical diffusivity D in the model, is the diffusion coefficient of dissolved cations in an average sense. Although this is a major simplification of the electrochemistry and the transport process, as mentioned earlier, this minimalistic view is able to reproduce the main characteristics of crevice corrosion damage (see Fig. 10 in the results section, and also [31–33,45]). Eq. (2) requires solid-solid bonds (bonds connecting two solid points) to have $k=0$, implying that no mass transfer in the metal phase is considered. For *interfacial* bonds that connect solid and liquid points and cross the solid-liquid interface $(\boldsymbol{x},\hat{\boldsymbol{x}},t) = k_{\mathrm{diss}}$, where k_{diss} denotes the micro-dissolvability, a parameter that controls the dissolution rate and is calibrated to the current density (i). We use a numerical calibration procedure to find the correlation between k_{diss} and i. This process is described in Section 2.2.3.

Different corrosion types can be modeled via defining the appropriate formula for current density according to the particular anodic dissolution kinetics of the desired corrosion type. For example, pitting [31,33,45], intergranular [32], stress-dependent [37,38], and galvanic corrosion [27], are respectively modeled by defining i as a function of concentration, various solid phases, deformation, and electric potential. In Section 3, we discuss how to define k_{diss} for crevice corrosion.

The damage index that defines phases in Eq. (2), is determined from Eq. (3). To use this definition of d, one needs to consider the mechanical bonds between solid points. Eqs. (3) and (4) state that d at a point $\boldsymbol{x}$ is equal to the number of intact mechanical bonds, divided by the total number of mechanical bonds connected to $\boldsymbol{x}$. In order to model the corrosion-induced damage in time, as the anodic dissolution takes place by the mass transfer from solid to liquid, one breaks mechanical bonds accordingly. To this aim, the concentration-dependent damage (CDD) model in Eq. (5) is used, to give an *expected* damage index d_c proportional to the concentration drop at the solid points near the interface (solid points that are connected to liquid points via interfacial dissolution bonds) [27]. In Eq. (5), C_{solid} is the molar concentration of pristine metal, equal to the molar mass divided by mass density. C_{sat} is the saturation concentration: the maximum possible concentration of metal ions in the electrolyte. Once d_c is found by Eq. (5), one then uses a stochastic procedure to break the mechanical bonds accordingly. This is achieved by randomly assigning $\mu(\boldsymbol{x},\hat{\boldsymbol{x}},t)=0$ for the bonds of $\boldsymbol{x}$, such that d in Eq. (3) is approximately equal to d_c from Eq. (5). One then updates the solid to liquid phase-change by updating d using Eqs. (3) and (4). The stochastic bond-breaking procedure was introduced in [30], and is briefly reviewed in Section 2.2.2, where the discretization method is presented.

It is noteworthy to say that this model results in a corrosion front with a δ-thick graded damaged layer in the solid phase, because of the bonds that have one leg in the solid and the other in the electrolyte. This solid layer is referred to as the *dissolving solid* as opposed to the *intact* solid being the rest of the solid phase (see Fig. 2). The intact solid (solid region more than one horizon away from the corrosion front) does not need to participate in the calculations (see below).The dissolving solid region has also a graded metal concentration between C_{solid} and C_{sat}, and is similar to the partially damaged/dissolved subsurface layer experimentally observed in different corroding metals [46–50]. This layer is weaker than the bulk metal (intact solid) and is a potential site for the initiation of cracks under mechanical loading. PD corrosion models naturally capture this corrosion-induced embrittlement [38,48].

2.2.2. Discretization

For the numerical discretization of the model presented in the previous section, we employ a quadrature-based meshfree method [51]. We first discretize the domain with a uniform grid (see Fig. 3):

Let N be the total number of nodes/grids. The PD integral can be approximated by mid-point (one-point Gaussian) quadrature as

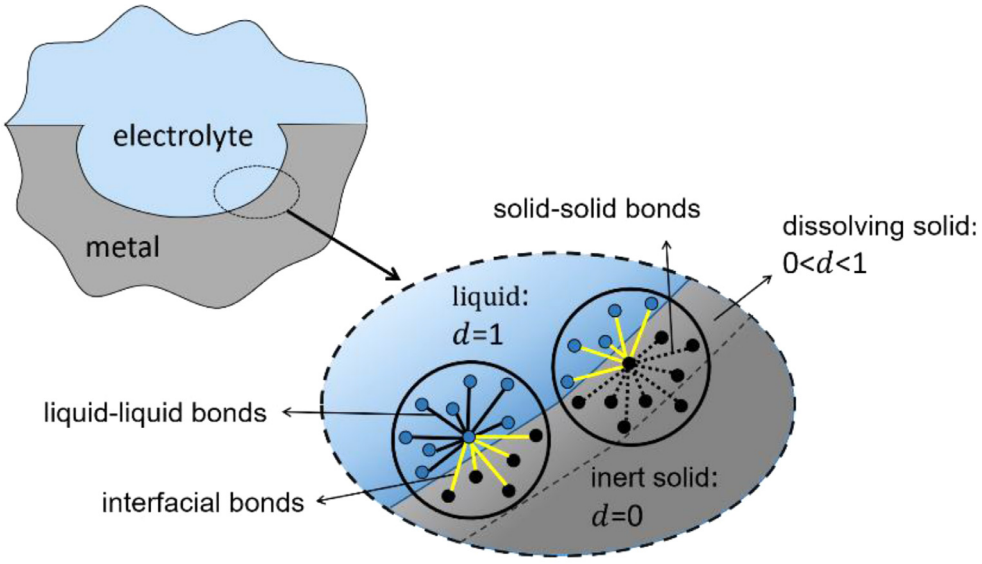

Fig 2. Schematics of a PD corrosion domain with focus on the solid-liquid interface and the three different types of PD bonds: solid-solid, liquid-liquid, and solid-liquid (interfacial) bonds [33].

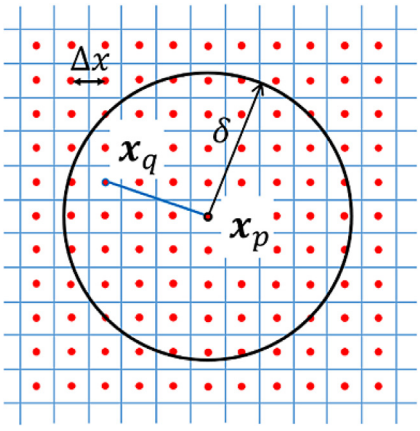

Fig 3. Discretization of space using uniform grid spacing (from [37]).

follows:

$$\frac{dC}{dt}(\boldsymbol{x}_p,t)=\sum_{\boldsymbol{x}_q\in H_{\boldsymbol{x}_p}} k(\boldsymbol{x}_p,\boldsymbol{x}_q,t)\frac{C(\boldsymbol{x}_q,t)-C(\boldsymbol{x}_p,t)}{|\boldsymbol{x}_q-\boldsymbol{x}_p|^2}\Delta V_{pq};\ \ p=1,2,\ldots,N \tag{7}$$

where $\boldsymbol{x}_p$ denotes the position vector for node p, and ΔV_{pq} is the volume (area in 2D) of the node $\boldsymbol{x}_j$ that is covered by the horizon of $\boldsymbol{x}_p$. While for most family nodes, $\Delta V_{pq}=\Delta x^2$ (in 2D), there are nodes near the horizon edge whose volumes are not fully covered by the horizon of $\boldsymbol{x}_p$. We use Eq. (8) to approximate ΔV_{pq} in 2D [52]:

$$\Delta V_{pq}=\begin{cases}\Delta x^2 & ,\ \text{if } |\boldsymbol{x}_q-\boldsymbol{x}_p|\le\left(\delta-\frac{\Delta x}{2}\right)\\ \left[\frac{\left(\delta+\frac{\Delta x}{2}\right)-|\boldsymbol{x}_q-\boldsymbol{x}_p|}{\Delta x}\right]\Delta x^2 & ,\ \text{if } \left(\delta-\frac{\Delta x}{2}\right)<|\boldsymbol{x}_q-\boldsymbol{x}_p|\le\left(\delta+\frac{\Delta x}{2}\right)\\ 0 & ,\ \text{if } \left(\delta+\frac{\Delta x}{2}\right)<|\boldsymbol{x}_q-\boldsymbol{x}_p|\end{cases} \tag{8}$$

We use a first-order ODE solver for integrating in time. In previous studies, explicit Forward Euler has been used for this purpose. However, in explicit schemes, the size of time steps is restricted by stability conditions. In problems were the diffusion in the electrolyte is important, the large diffusion coefficient of the electrolyte restricts the time step to very small values, and therefore, computations for relatively long corrosion times would be very costly with explicit time marching. In this study, we use the implicit backward Euler for time integration which is stable for any time step size [53]:

$$\frac{C_p^{n+1}-C_p^n}{\Delta t}=\sum_{\boldsymbol{x}_q\in H_{\boldsymbol{x}_p}} k_{pq}\left(d_p^n,d_q^n\right)\frac{C_q^{n+1}-C_p^{n+1}}{|\boldsymbol{x}_q-\boldsymbol{x}_p|^2}\Delta V_{pq};\ \ p=1,2,\ldots,N \tag{9}$$

The subscripts p and q refer to the nodal coordinates x_p and x_q and the superscripts n and $n+1$ refer to the current and next time steps (t^n and $t^{n+1}=t+\Delta t$) respectively. In Eq. (9) we use d at the time step t^n, not t^{n+1}, which means that the phase-change process is explicit, while the transport is solved implicitly.

At each time step, Eq. (9) updates the concentration field, and d_c^{n+1} is computed for each node from Eq. (5). Then, the following stochastic algorithm is used for breaking mechanical bonds accordingly [30]:

- For each node $\boldsymbol{x}_i$ compute the *probability of bond breaking* $P_p^{n+1}=\frac{1}{1-d_c^{n+1}}\left(\frac{C_p^n-C_p^{n+1}}{C_{\text{solid}}-C_{\text{sat}}}\right)$;
- For each intact mechanical bond connected to $\boldsymbol{x}_i$, generate a random number from a uniform distribution in $(0,1)$;

  - If this random number is smaller than P_p^{n+1}, then break this mechanical bond: $\mu_{pq}^{n+1}=0$;

After bond breaking, d_i^{n+1} is updated from:

$$d_p^{n+1}=1-\frac{\sum_{\boldsymbol{x}_q\in H_{\boldsymbol{x}_p}}\mu_{pq}^{n+1}}{\sum_{\boldsymbol{x}_q\in H_{\boldsymbol{x}_p}}1};\ \ p=1,2,\ldots,N \tag{10}$$

which is the discrete version of Eq. (3). d_p^{n+1} is then used to identify the nodal phase at the next time step.

Note that to improve efficiency, while the nodes located in the "intact solid" region are "present" in the simulation, they do not participate in the computations for the time steps when they belong to that region. The reason is that the micro-diffusivity for solid-solid bonds is zero, and the summation (right-hand side of Eq. (9)) for these nodes will be zero. As the liquid phase advances, some nodes in the intact solid region will start having nodes in their family that are "liquid phase" and therefore, they become

a part of the dissolving region and will start participating in the computations from that moment on.

2.2.3. Numerical calibration of micro-dissolvability

As mentioned in the previous section, micro-dissolvability is numerically calibrated to the anodic current density. The following relationship is assumed between k_{diss} and i [33]:

$$k_{\text{diss}} = \left(\frac{k_{\text{diss}}^{\text{trial}}}{i^{\text{trial}}}\right) i \tag{11}$$

where i^{trial} is the current density obtained from a trial PD simulation assuming an activation-controlled uniform corrosion with $k_{\text{diss}} = k_{\text{diss}}^{\text{trial}}$, a trial micro-dissolvability. Activation controlled condition here is modeled by setting the $C(\boldsymbol{x}, t) = 0$ everywhere in the electrolyte region [30]. This eliminates the dependency of the dissolution rate on the transport in the electrolyte and $k_{\text{diss}}^{\text{trial}}$ becomes the only parameter that controls the corrosion rate. Note that the choice of horizon size and spatial discretization size in the trial simulation should be the same as the ones in the main simulation. For more details on trial simulation please see [30,31]. The current density from a trial simulation can be computed using Faraday's second law:

$$i^{\text{trial}} = zF \frac{\sum_{j=1}^{N} \left[C(\boldsymbol{x}_j, 0) - C(\boldsymbol{x}_j, t)\right] \Delta V_j}{At} \tag{12}$$

where z is the charge number, F is the Faraday's constant, A is the corroding area, t is the corrosion time, N is the total number of nodes in the domain, and ΔV_j is the nodal volume at $\boldsymbol{x}_j$. The numerator in Eq. (12) gives the total mass loss due to anodic dissolution from the initial time until time t. Division by At gives the dissolution mass flux which can be translated into current density by multiplying with zF.

Once Eq. (11) is used to define k_{diss} in Eq. (2) in terms of the current density i, any type of corrosion can be modeled using the particular formula for the current density specific to the local anodic dissolution kinetics for that particular corrosion type. This approach was used in PD corrosion models for predict pitting [31,33,45], intergranular [32], galvanic [27], and stress-dependent [37,38] corrosion, with the only difference in these models being the different k_{diss} (from different current densities) formulas. In the present study, we will establish a relationship for k_{diss} for crevice corrosion damage, based on the underlying electro-chemo-physics.

3. Peridynamic crevice corrosion model

In this section, we introduce the new PD model for crevice corrosion damage. To this aim, based on the underlying electro-chemo-physics of crevice corrosion, we construct a formula for k_{diss} that effectively reproduces the kinetics of anodic dissolution inside crevices.

Crevice corrosion is known to be driven by the local environmental changes inside the crevice [1]. The steps involved in the dominant mechanism are: 1) restricted flow of electrolyte in the crevice results in accumulation of dissolved positively charged metal ions, produced by anodic dissolution, either by metastable pits in passive alloys, micro-galvanic corrosion induced by impurities and inclusions on the metal surface inside the crevice, or activation due to IR-drop inside the crevice [54–56]; 2) electroneutrality causes migration of chloride (or other aggressive anions) from the bulk electrolyte into the crevice; 3) as a result, hydrolysis reaction increases, and pH drops; 4) local acidification in the crevice increases the anodic dissolution rate which produces more positively charged ions at a faster rate. These steps are then repeated. Fig. 4(a) shows these four steps in the crevice corrosion mechanism. This self-accelerating dissolution process is restricted by saturation of the electrolyte and salt layer formation that may occur due to the slow mass transfer in the crevice (diffusion path is long and narrow). In locations along the crevice where the electrolyte is saturated (usually near the closed end), anodic dissolution is controlled by the mass transfer and therefore follows a diffusion-controlled regime [1].

The self-accelerating dissolution process and its restriction by saturation of the electrolyte, can be simplified in the following statement: *the local corrosion rate increases as the concentration of dissolved metal ion increases, up to saturation of electrolyte*. Fig. 4(c) shows this simplified interpretation. Consequently, one can describe the local anodic current density $i(\boldsymbol{x}, t)$ as a function of the local metal ion concentration:

$$i(\boldsymbol{x}, t) = \begin{cases} f[C(\boldsymbol{x}, t)] & C(\boldsymbol{x}, t) < C_{\text{sat}} \\ zFJ(\boldsymbol{x}, t) & C(\boldsymbol{x}, t) = C_{\text{sat}} \end{cases} \tag{13}$$

where f is an increasing function of C, and $J(\boldsymbol{x}, t)$ is the diffusion flux at point $\boldsymbol{x}$ on the corrosion front and time t, and z and F are given after Eq. (12) (see above). Note that in this model we are neglecting the flux caused by electromigration and advection.

Using Eqs. (11) and (13), and knowing that the PD corrosion model provides the evolution of metal ion concentration in the electrolyte, we define k_{diss} to be a metal ion concentration-dependent quantity:

$$k_{\text{diss}}(\boldsymbol{x}_{\text{S}}, \boldsymbol{x}_{\text{L}}, t) = \begin{cases} \left(\frac{k_{\text{diss}}^{\text{trial}}}{i^{\text{trial}}}\right) f[C(\boldsymbol{x}_{\text{L}}, t)] & C(\boldsymbol{x}_{\text{L}}, t) < C_{\text{sat}} \\ 0 & C(\boldsymbol{x}_{\text{L}}, t) \geq C_{\text{sat}} \end{cases} \tag{14}$$

where $\boldsymbol{x}_{\text{S}}$ and $\boldsymbol{x}_{\text{L}}$ are respectively the solid and the liquid ends of an interfacial bond. For any specific corrosion system, i.e. metal and environment, C_{sat} and the function $f(C)$ need to be determined. C_{sat} is a quantity that can be found in the literature. $f(C)$ however, is a new concept and no standard methods for obtaining it exist. Inspired by [26], the approach that we use in this work to obtain $f(C)$ is the following:

1) Find the relationship between anodic current density and pH at a given potential: i(pH), using polarization curves measured at different pH values.
2) Substitute the pH in the relationship, with mathematical models and/or empirical equations that calculate the pH in terms of concentration of metal ions: pH(C).

This two-step process is the same as the one plotted in Fig. 4(b). In the example in Section 5, we show that this procedure works in a specific case.

In order to model the diffusion-controlled regime [57] when C reaches C_{sat} near the interface, we approximate the balance between corrosion and diffusion rates by temporarily pausing dissolution (mass transfer through the bonds that have one end in the solid and the other in the saturated electrolyte). To accomplish this, we *temporarily* set these bonds' micro-diffusivity to zero: $k_{\text{diss}} = 0$. Once diffusion in the electrolyte leads to a drop in concentration below C_{sat}, the dissolution re-starts, and the appropriate bonds are reassigned the non-zero k_{diss} values computed from Eq. (14). This means that we are essentially approximating the continuous diffusion-controlled corrosion process by a piecewise constant function, where the dissolution is effectively slowed down by a sequence of pauses and releases, such that the overall rate is balanced with the diffusion flux in the electrolyte. This removes the need for modeling the salt layer formation explicitly, as well as that of computing the diffusion flux near the interface (which would require us to track the interface and integrate locally to compute the flux). This choice makes our model very efficient and autonomous, as no explicit interface tracking needed. For more details on the PD salt-layer model for pitting corrosion, please see [31,33].

Note that the concentration field variable C in the model and $[M^{+z}]$ in Fig. 4, only pertains to the metal ions dissolved from

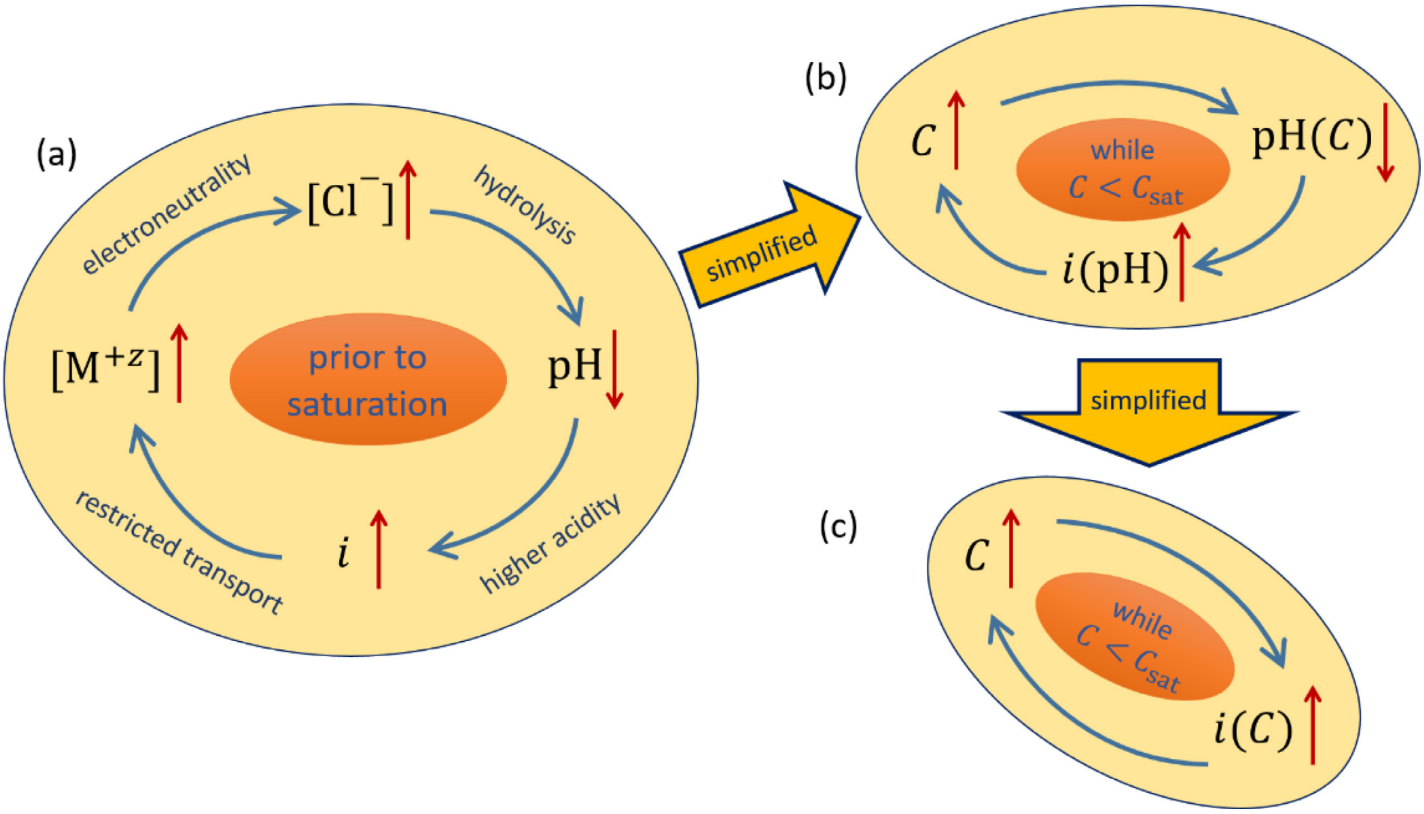

Fig 4. Self-accelerating anodic dissolution mechanism in crevice corrosion: (a) the 4-step cycle, where $[M^{+z}]$ is the concentration of positively charged metal ions, i.e. C, and $[Cl^-]$ denotes the concentration of chloride; (b) 3-step equivalent cycle with a concentration dependent pH, and a pH-dependent current density; (c) a 2-step simplified version with a concentration-dependent current density.

the corroding substrate and does not consider other possibly existing cations in the electrolyte such as Na^+. The model adopts this simplified approach because the effects on dissolution of the solid phase (our primary interest) from these cations is likely small. Moreover, the model can be extended to include various chemical species, if desired, by considering distinct concentration fields for as many chemical species as needed and solve for their transport. Electrostatics can also be coupled with transport solvers (e.g., see our recent paper on galvanic corrosion [27]) to find the electric potential profile and investigate the ohmic drop in the crevice. Obviously, such an approach would increase the computational complexity significantly, for a potentially minor increase in accuracy.

Despite its simplicity, the proposed minimalistic model is a fairly general approach for simulating crevice corrosion. A variety of metallic compounds, electrolytes, chemical species, temperatures, etc., can be covered in the model by obtaining appropriate relationships that describe the particular corrosion rate as a function of the local metal ion concentration value, for specific material and environmental conditions. This is possible because the concentration-dependent current density is able to model the local acidification, caused by the slow mass transfer (the dominant crevice corrosion mechanism), regardless of the particular material composition and electrolyte present. The specifics of the concentration-dependent current density relationship however, depends on the particular system studied (metal, electrolyte, chemicals, etc.), and it can come from experiments or theoretical models for each specific problem.

As mentioned in the introduction, while some differences between crevice corrosion in passive and non-passive metals exist, local acidification due to slow mass transfer is the main mechanism for both types of metal. As a result, the new PD model can be tailored to simulate crevice corrosion in metals with or without passive films.

4. Modified PD formulation for using discretization grids with extreme aspect ratios

The extreme aspect ratio of the geometry in crevices (long and narrow) present a significant computational challenge: if the same spacing is used in a uniform domain discretization, the computational cost may be too large; therefore, a discretization that matches the geometry aspect ratio (large spacing along the long direction, and small spacing along the short direction) is desirable. Using such a grid with the standard PD formulation (with spherical horizon) would not work, since we may leave covering nodes only in the dense direction, and no nodes in the coarse direction. Note also that to reduce grid dependency and have an acceptable accuracy in the quadrature used for computing the PD integral, grid spacing should not be larger than ¼ or, at most, 1/3 of the horizon size [58]. On the other hand, it is well understood that the horizon size should be smaller than the smallest geometrical feature of the domain to prevent undesired/unrealistic nonlocal effects [59]. For crevice corrosion, using the spherical horizon, this means that δ has to be several times smaller than the gap size.

To resolve this issue, we introduce the PD formulation for *non-spherical horizons* (or non-circular in 2D) so that it can work with grids that have extremely different grid densities in different directions.

Note that, for noncircular horizon, $k(\boldsymbol{x}, \boldsymbol{x}', t)$ in Eq. (1) cannot be computed from Eq. (2), because that relationship is obtained by a calibration process that assumed a spherical/circular horizon. We propose the following modification to Eq. (2) for noncircular

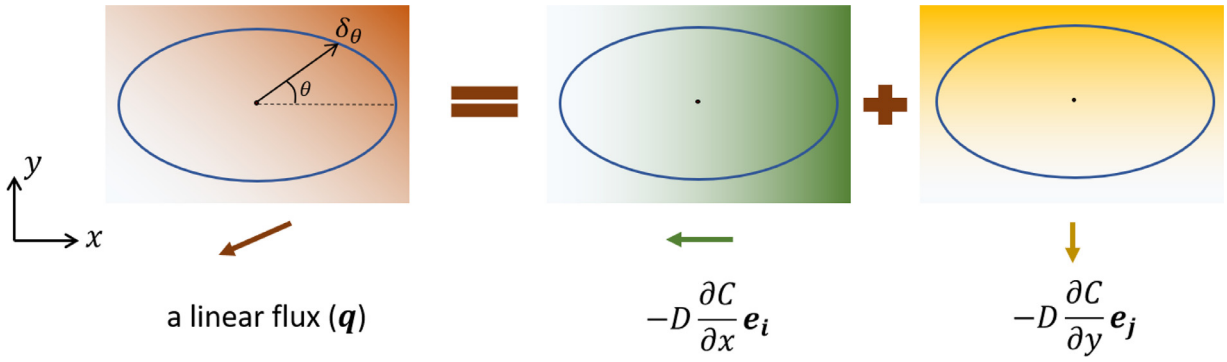

Fig 5. A linear concentration profile (a constant flux) and its projections into x and y coordinates; an elliptical PD horizon as an example for demonstration of a non-spherical horizon; and the direction-dependent nonlocality range (δ_θ).

horizons:

$$k^\theta\left(\boldsymbol{x},\hat{\boldsymbol{x}},t\right)=\begin{cases} k_{\mathrm{L}}^\theta(D,\delta_\theta) & ,d(\boldsymbol{x},t)=1 \text{ and } d\left(\hat{\boldsymbol{x}},t\right)=1 \\ 0 & ,d(\boldsymbol{x},t)<1 \text{ and } d\left(\hat{\boldsymbol{x}},t\right)<1 \\ k_{\mathrm{diss}}^\theta & ,d(\boldsymbol{x},t)=1 \text{ xor } d\left(\hat{\boldsymbol{x}},t\right)=1 \end{cases} \tag{15}$$

where δ_θ is the nonlocality range along the bond direction that makes an angle θ with the x-axis (polar angle). In 3D, the direction is given by the spherical coordinates, and in 1D, δ_θ has only two values along the positive and the negative coordinate directions. $k_{\mathrm{L}}(D,\delta_\theta)$ is computed from Eq. (16) which is obtained by replacing δ in Eq. (6) with δ_θ. This makes the micro-diffusivity a direction dependent quantity, in order to match a given direction-independent diffusivity constant D:

$$k_{\mathrm{L}}(D,\delta_\theta)=\begin{cases} \frac{D}{\delta_\theta} & ,1\mathrm{D} \\ \frac{4D}{\pi{\delta_\theta}^2} & ,2\mathrm{D} \\ \frac{9D}{\pi{\delta_\theta}^3} & ,3\mathrm{D} \end{cases} \tag{16}$$

We now show that the new formulation is consistent with classical isotropic diffusion for the 2D case. Similar proofs can be carried out for the 1D and 3D cases as well.

In [60], the calibration of k in PD diffusion with spherical horizons is carried out by finding k such that the classical flux ($\boldsymbol{q}_{\mathrm{classic}}$) and the peridynamics flux ($\boldsymbol{q}_{\mathrm{Peri}}$) are equal for a linear concentration (constant flux) profile. Below, we follow similar steps to show that Eq. (16) is a valid calibration of k for PD diffusion equation with arbitrary (non-spherical) horizon.

For homogeneous isotropic diffusion the classical flux is given by:

$$\boldsymbol{q}_{\mathrm{classic}}=\ -D\nabla C=-D\left(\frac{\partial C}{\partial x}\boldsymbol{e_i}+\frac{\partial C}{\partial y}\boldsymbol{e_j}\right) \tag{17}$$

where ∇ denotes the gradient operator, and $\boldsymbol{e_i}$ and $\boldsymbol{e_j}$ are the unit vectors in x and y Cartesian directions. According to [60], PD flux can be defined by:

$$\boldsymbol{q}_{\mathrm{peri}}=-\int_{\mathcal{H}_x^+} k\frac{C\left(\hat{\boldsymbol{x}},t\right)-C(\boldsymbol{x},t)}{\left|\hat{\boldsymbol{x}}-\boldsymbol{x}\right|}\boldsymbol{e}_{\hat{\boldsymbol{x}}}\,\mathrm{d}V_{\hat{\boldsymbol{x}}} \tag{18}$$

where $\mathcal{H}_x^+$ is the part of the horizon with $C(\hat{\boldsymbol{x}},t)>C(\boldsymbol{x},t)$, and $\boldsymbol{e}_{\hat{\boldsymbol{x}}}$ is the unit vector along the bond $\hat{\boldsymbol{x}}-\boldsymbol{x}$.

We consider a linear profile for $C(\boldsymbol{x},t)$, and an arbitrary-shape horizon for the PD integral (see Fig. 5).

By projecting the linear concentration gradient into the Cartesian coordinates as shown in the Fig. 5, the PD flux can be expressed as:

$$\boldsymbol{q}_{\mathrm{peri}}=-\boldsymbol{e_i}\int_{-\frac{\pi}{2}}^{\frac{\pi}{2}}\int_0^{\delta_\theta} k\frac{C\left(\hat{\boldsymbol{x}},t\right)-C(\boldsymbol{x},t)}{\left|\hat{x}-x\right|}\cos^2\theta\ r\mathrm{d}r\mathrm{d}\theta-\boldsymbol{e_j}\int_0^{\pi}\int_0^{\delta_\theta} k\frac{C\left(\hat{\boldsymbol{x}},t\right)-C(\boldsymbol{x},t)}{\left|\hat{y}-y\right|}\sin^2\theta\ r\mathrm{d}r\mathrm{d}\theta \tag{19}$$

We substitute k, with the formula given by Eq.(16):

$$\boldsymbol{q}_{\mathrm{peri}}=-\boldsymbol{e_i}\int_{-\frac{\pi}{2}}^{\frac{\pi}{2}}\int_0^{\delta_\theta}\frac{4D}{\pi\delta_\theta^2}\frac{C\left(\hat{\boldsymbol{x}},t\right)-C(\boldsymbol{x},t)}{\left|\hat{x}-x\right|}\cos^2\theta\ r\mathrm{d}r\mathrm{d}\theta-\boldsymbol{e_j}\int_0^{\pi}\int_0^{\delta_\theta}\frac{4D}{\pi\delta_\theta^2}\frac{C\left(\hat{\boldsymbol{x}},t\right)-C(\boldsymbol{x},t)}{\left|\hat{y}-y\right|}\sin^2\theta\ r\mathrm{d}r\mathrm{d}\theta \tag{20}$$

Given that $C(\boldsymbol{x},t)$ profile is linear, one can write:

$$\boldsymbol{q}_{\mathrm{peri}}=-D\frac{\partial C}{\partial x}\boldsymbol{e_i}\int_{-\frac{\pi}{2}}^{\frac{\pi}{2}}\int_0^{\delta_\theta}\frac{4}{\pi\delta_\theta^2}\cos^2\theta\ r\mathrm{d}r\mathrm{d}\theta-D\frac{\partial C}{\partial y}\boldsymbol{e_j}\int_0^{\pi}\int_0^{\delta_\theta}\frac{4}{\pi\delta_\theta^2}\sin^2\theta\ r\mathrm{d}r\mathrm{d}\theta=-D \tag{21}$$

As shown above, using the proposed direction dependent micro-diffusivity in Eq. (16) recovers the classical flux for isotropic diffusion in 2D. This formulation works for any horizon shape. The elliptical horizon in Fig. 5, is just an example for demonstration.

Note that the non-spherical horizon in this study does not lead to anisotropic behavior as it may in other studies (e.g., [61]). The reason is that k_{L}^θ here is calibrated for an isotropic classical model. From a physical point of view, the direction dependent micro-diffusivity in Eq. (16) has a lower value in directions where δ_θ is larger, and a higher value in directions where δ_θ is smaller. This leads to a balanced transport in all directions (at the continuum level), and isotropy is maintained.

Now we derive the direction-dependent micro-dissolvability k_{diss}^θ in Eq. (15) for a non-spherical horizon. Assume PD diffusion with a spherical horizon of radius δ_{ref}. Given Eqs.(6) and (16), one can write $k_{\mathrm{L}}^\theta=k_{\mathrm{L}}(\frac{\delta_{\mathrm{ref}}}{\delta_\theta})^n$ where $n=1,2,3$ for 1D, 2D,and 3D, respectively. This means that one can use a k that is calibrated for the spherical horizon with $\delta=\delta_{\mathrm{ref}}$, in a model with non-spherical horizon, by multiplying the flow density in Eq. (1) by $(\frac{\delta_{\mathrm{ref}}}{\delta_\theta})^n$. This implies that we can write:

$$k_{\mathrm{diss}}^\theta=\ k_{\mathrm{diss}}\left(\frac{\delta_{\mathrm{ref}}}{\delta_\theta}\right)^n \tag{22}$$

where k_{diss} is a micro-dissolvability calibrated for a spherical horizon with the radius δ_{ref} (see Section 2.2.3 for calibration of k_{diss}).

Note that Eq. (6), and consequently Eqs. (16) and (22), are derived for the particular kernel used in the PD integral in Eq. (1). If the PD diffusion equation uses another kernel (e.g. see [58,62]), one needs to modify all derivations accordingly.

For the crevice corrosion simulation presented in the next section, we use an elliptical horizon with the long axis aligned with the crevice length direction, and the short axis along the crevice gap direction. This will allow us to choose coarse grid spacing in the crevice length direction and dense grid spacing in the crevice gap direction.

5. Model validation

Here we validate the PD crevice corrosion model described in Section 3 against the experimental results shown in [42].

5.1. Brief description of experimental setup

In an experiment reported in [42], two washers were held together using a nut and bolt fastener (see Fig. 6(a)). The washers, bolt, and nut were all made of Nickel alloy 625. The bolted washers were immersed in ASTMartificial ocean water at room temperature, and potentiostatic tests were carried out at 200 mV (vs SCE). The experimental study focused on the crevice corrosion propagation between the washers [42].

5.2. Model input data and the calibration of concentration-dependent k_{diss}

The input data for our PD model of crevice corrosion are discussed next. The major elements (> 1 wt%) of alloy 625 are Ni, Cr, Fe, Mo, and Nb, resulting in Ni2+, Cr3+, Fe2+, Mo3+, and Nb5+ cations during corrosion. According to [42], the corresponding salts that precipitate when saturation occurs are NiCl2, CrCl3, FeCl2, MoCl3, and [(0.5)Nb2O5 + (5)HCl]. As noted earlier, our simplified, minimalistic model uses a single variable C to collectively represent the concentration of all alloy's elements in the solid phase and the corresponding dissolved cations in the liquid phase (electrolyte). Molar concentration of the pristine metal can be approximated by dividing the alloy's mass density over its molar mass: $C_{\text{solid}} = 140$ M. Saturation concentration of the alloy in the electrolyte used here is reported to be $C_{\text{sat}} = 5.6$ M [26]. The diffusion coefficient of metal ions in the electrolyte used in the experiment is $D = 720\ \mu\text{m}^2/\text{s}$ [42]. To find the concentration-dependent k_{diss} formula for this metal-electrolyte system, one first needs to determine the anodic current density as a function of metal ions' concentration. To this aim, we follow the procedure described in Section 3. From published polarization curves carried out at different pH levels [26], we read the current density values associated with different pH values at $E = 200$ mV (SCE). Using Matlab's curve fitting toolbox, we fit an exponential function to these data points. Fig. 7 shows the experimental data points read from [26] and the fitted function.

The fitted function gives i (A/cm^2) as a function of pH:

$$\log(i) = 1.151 \exp(-723\text{pH}) - 7.647 \tag{23}$$

Note that the current density varies along the interface, depending on the *local* pH value at the interface. In absence of specific interfacial pH values for the crevice, for simplicity, the pH values we used here to find the relationship between the anodic current density and pH, at an arbitrary point along the crevice, are those shown in the polarization curves in [26], measured in the bulk, for an open surface [63]. Such values should not differ too much from the interfacial pH values for the open surface case.

The experimental data points in Fig. 7, imply that the activation of the passive sites occurs at low pH values. Given the limited number of data points (only five), the fitted exponential function is a reasonable interpolation that allows one to continuously determine the corrosion rate across a wide range of pH values. Current densities as low as $10^{-7.5}$ A/cm^2 (close to passivation current densities) at high pH, and higher current densities (10^{-7} to 10^{-4} A/cm^2) at lower pH values are all captured by this function.

In the same study [26], pH is provided in terms of metal ions concentration from electrochemical and phenomenological relationships between species. Fitting a function to such data points provides pH as a function of C(M) (see Fig. 8):

$$\text{pH} = 7.405 \exp(-0.08036\ C) - 6.498 \tag{24}$$

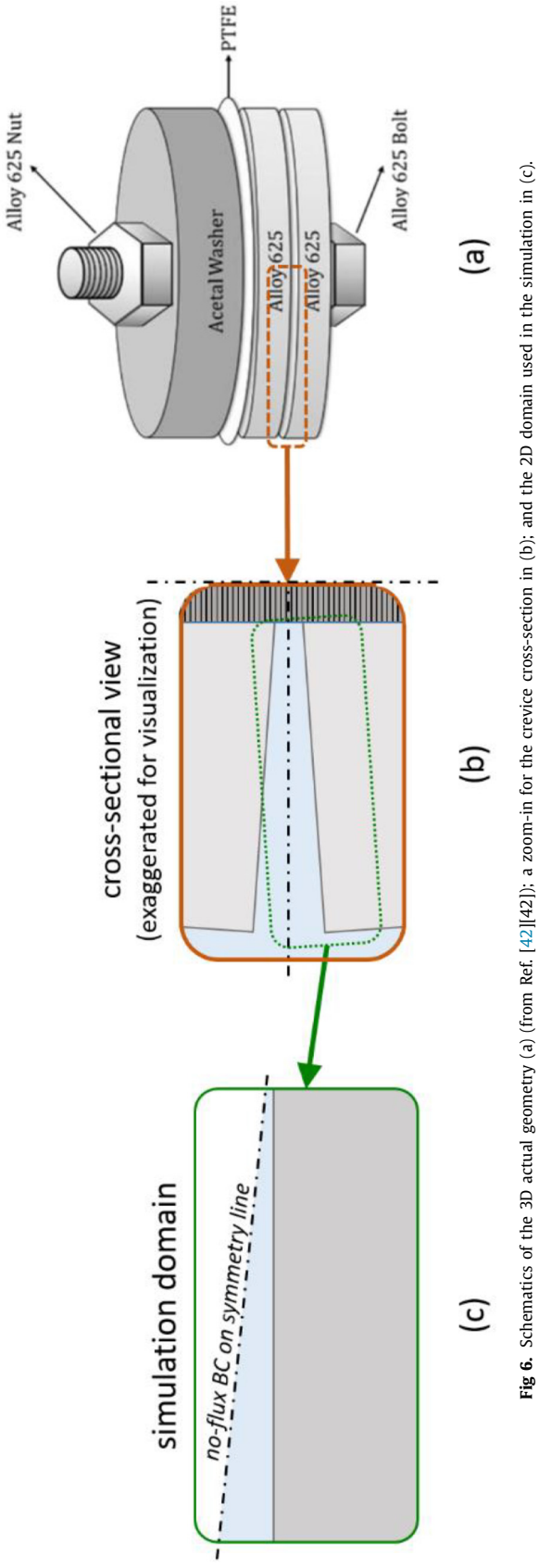

Fig 6. Schematics of the 3D actual geometry (a) (from Ref. [42][42]); a zoom-in for the crevice cross-section in (b); and the 2D domain used in the simulation in (c).

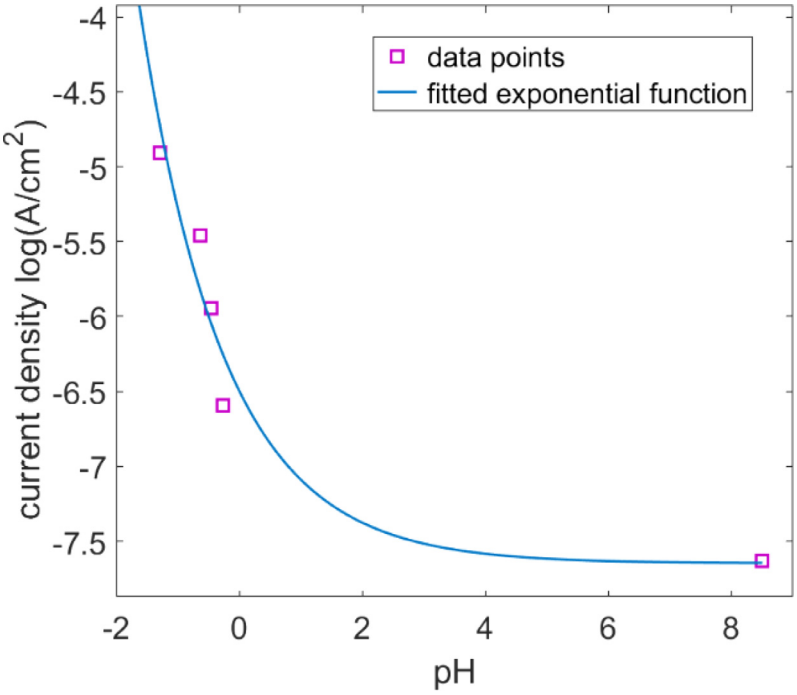

Fig 7. Anodic current density in logarithmic scale in terms of pH value at 200 mV (SCE). Data points are collected from polarization curves given in [26].

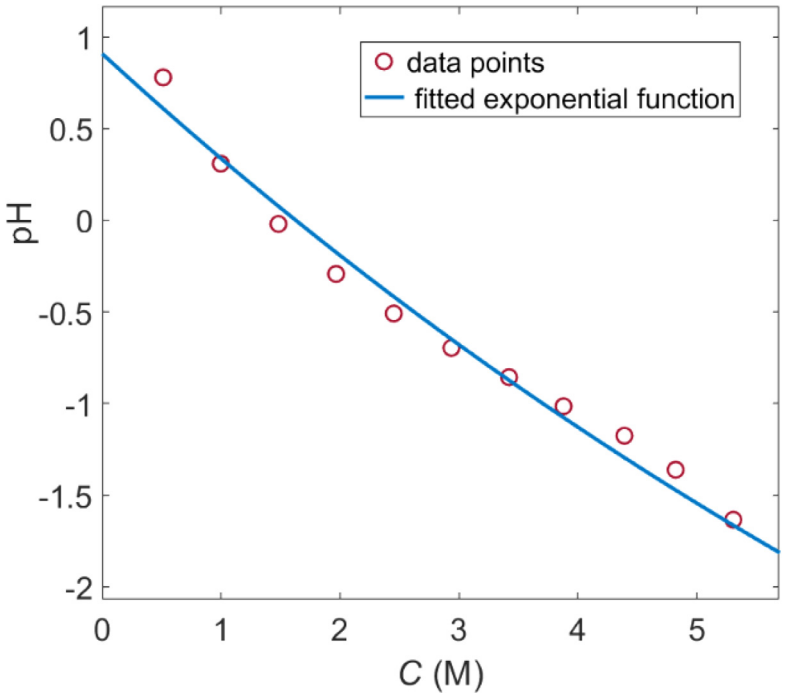

Fig 8. The pH values in terms of dissolved metal concentration (from [26]), and the fitted exponential function given in Eq. (24).

where C is in mol/m^3. Substituting pH in Eq. (23) with the function in Eq. (24), we find:

$$i(C) = 10^{1.151\exp\{-723[7.405\exp(-0.08036\ C)-6.498]\}-3.647} \tag{25}$$

where i is in A/m^2.

As discussed in the procedure explain in Section 2.2.3, we calibrate k_{diss} to i by using a trial simulation of a uniform corrosion that assumes a trial micro-dissolvability. The trial simulation using a spherical horizon with $\delta = 4\ \mu$m and uniform grid spacing $\Delta x = \Delta y = 1\ \mu$m with $k_{\text{diss}}^{\text{trial}} = 0.04\ \mu\text{m}^{-1}$ results in $i^{\text{trial}} = 2.22 \times 10^4$ A/m^2. Using Eq. (14) gives:

$$k_{\text{diss}}(\boldsymbol{x}_S, \boldsymbol{x}_L, t) = \begin{cases} \left(1.8 \times 10^{-6}\right) \times 10^{1.151\exp\{-723[7.405\exp(-0.08036\ C(\boldsymbol{x}_L,\ t))-6.49} \\ 0 \end{cases} \tag{26}$$

Note that in this example we used the pH-dependent polarization curves and the pH-concentration relationships because they were available to us from literature. One can use (or propose) any other experimental/analytical method that provides a reasonable relationship between anodic current density and metal ions con-

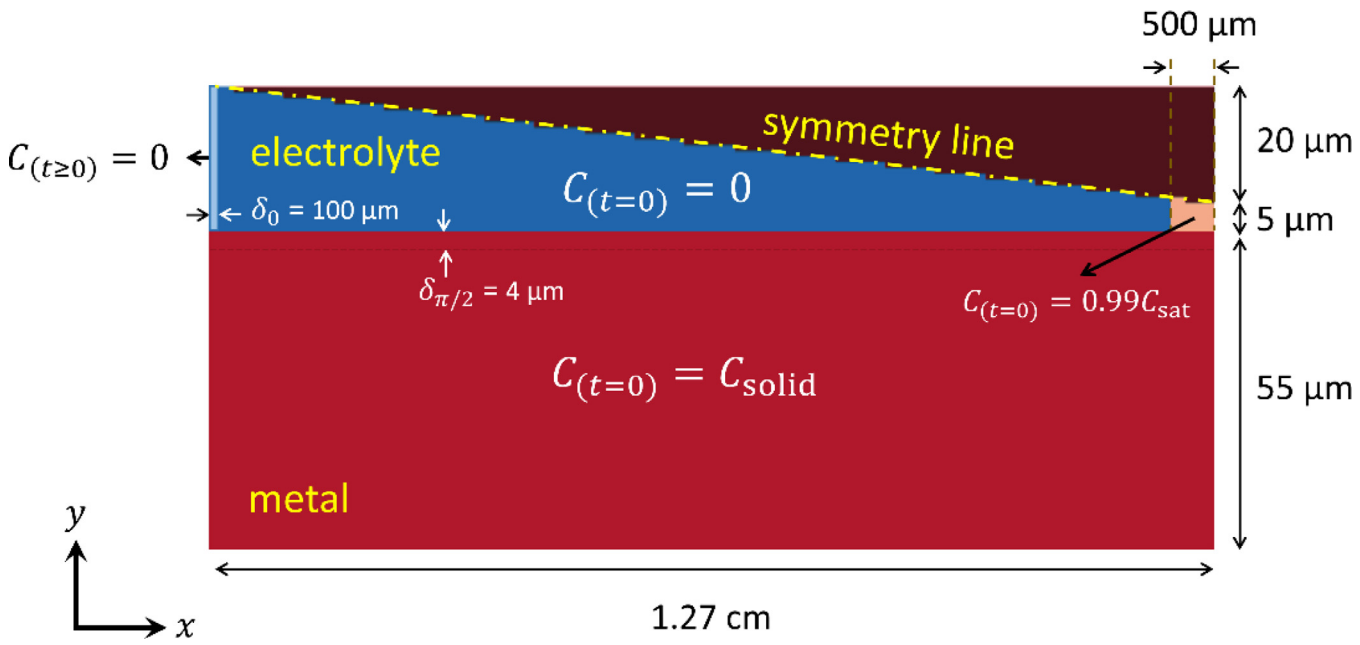

Fig. 9. Geometry of the 2D computational model, with the initial and boundary conditions. Note the different scales used in the horizontal and vertical directions.

centration to construct the concentration-dependent current density. For example, if data on corrosion rate in terms of chloride concentration is available, one can use the principle of electroneutrality to approximate the corresponding metal ions concentration (at a given chloride concentration) and find $i(C)$.

5.3. Computational model setup

We use a 2D peridynamic model of transverse cross-section of the washers to simulate the crevice corrosion in the system described in [42] (see Fig. 6). The crevice length is the radial distance from the inner hole to the outer edge of the washers, which is 1.27 cm. The experimental study [42] reports that "the values of crevice gap varied between 20 μm **near** the crevice tip, to 50 μm near the crevice mouth."(see page 99 of [42]). No measurements are reported for the gap at the very end of the crevice. It is reasonable to assume that the gap at the tip of the crevice is effectively narrower than the measured 20 μm near the tip. For these reasons we consider the following geometry for the computational model of the crevice: a wedge-shape crevice between the washers, with the length of 1.27 cm and the effective gap size of 50 μm at the mouth, and 10 μm at the tip. A similar geometry was considered in [26]. Note that the wedge shape of the gap is expected since the washers are under compression in their center by the bolt.

We use the symmetry of the geometry (washers are identical) to define the computational domain (see Fig. 6): a washer and the half of the wedge crevice with dimensions shown in Fig. 9. Fig. 6 shows how the 2D domain is chosen from the actual 3D geometry, and Fig. 9 also gives the initial and boundary conditions used. Note that across the symmetry line the flux is zero.

For the boundary conditions, we set $C = 0$ for a δ-thick layer at the crevice mouth to represent the connection to the bulk dilute electrolyte. The thickness is required because of the special way that nonlocal boundary conditions are defined in PD problems. Details on nonlocal boundary conditions are available in [64,65]. The rest of the boundaries (including the symmetry line) are free boundaries and the no-flux conditions is naturally satisfied.

Knowing that corrosion in passive alloys starts from distributed metastable pits [54,56], it is reasonable to assume that it is more likely for metastable pits to become stable near the end of the crevice due to the increased acidity and accumulation of ions. Note that our model, at this stage, does not include the initiation stage. Our focus is on the propagation phase, this is why we assume, at the start of the simulation, a highly concentrated region near the crevice's end, which is likely to occur during the initiation phase for this particular problem. If needed, these initial conditions can be adjusted as needed for other geometries/setups. The corrosion model, however, remains the same.

Therefore, we impose the following initial conditions (see Fig. 9): $C = C_{\text{solid}}$ over the washer region and $C = 0$ over the electrolyte region, except for a small area of width 500 μm at the crevice end where we impose $C = 0.99C_{\text{sat}}$. The nearly saturated electrolyte near the end causes a local spike in current density according to Eq. (26) near the closed end. The accumulated ions at the end acts as corrosion initiation at the tip of the crevice which could occur from stabilization of metastable pits near the end, or micro galvanic dissolution of or around metallic inclusions on the surface. The particular size of 500 μm is selected here because we found that this is approximately the minimum size that can trigger the self-propagating crevice corrosion process. The 500 μm value was found by trying several different widths from 100 to 1000 μm. Using values smaller than 500 μm, caused the metal-ion concentration to diffuse out quickly before the accumulation was able to sustain the self-accelerating cycle illustrated in Fig. 4.

As noticed from the dimensions shown in Fig. 9, the crevice length is two orders of magnitude larger than the gap. We use the PD formulation from Section 4 with an elliptical horizon so that grid spacing along the length can be selected to be 25 times larger than the spacing in the gap direction. We choose the elliptical horizon with $\delta_0 = 100$ μm and $\delta_{\pi/2} = 4$ μm (subscripts are the values for the polar angle θ) along the major and minor axes, respectively, and set grid spacings $\Delta x = 25\mu$m and $\Delta y = 1$ μm to discretize the domain. A measure of grid density inside the horizon for PD with spherical horizon and uniform grid spacing is the m-factor defined by $/\Delta x$. Note that in our case, the m-factor is direction-dependent, but given the choices shown above, for the horizontal and vertical directions, they are: $\delta_0/\Delta x = \delta_{\frac{\pi}{2}}/\Delta y = 4$. δ_{ref} and Δx in the calibration simulation are taken to be 4 μm and 1 μm, respectively.

Note that k_{ij} in the Backward Euler scheme (Eq. (9)), is obtained from Eq. (26) with C^{n+1}. This leads to a nonlinear system of equations in terms of C^{n+1}. We use a modified Polak-Ribiere nonlinear Conjugate Gradient method [66] to solve the nonlinear system at each time step. The total corrosion time to be simulated was 72 hours. We used a time step of $\Delta t = 5$ s.

5.4. Simulation results and discussion

Fig. 10 shows the PD simulation results in several snapshots in comparison with the corresponding experimental observations (at same times and using the same geometrical scales). The experimentally obtained graphs (left column, taken from [42]) for the corrosion profiles at different times were obtained by Optical Profilometry, scanning the depth along a radial line on the washer surface [42]. The PD simulation results (right column) monitor nodal damage and the metal ion concentration in the crevice. The PD snapshots use the same length scales as the ones employed for the experimental results from [42]. The window frame drawn on top of the first simulation snapshot is the corresponding window used for the experimental results shown in the left column. The PD simulation results are also provided in Video 1 (see Supplementary Materials).

The complex evolution of corrosion damage is predicted very well by the PD model. Damage starts at the closed end and moves towards the mouth as time passes, affecting only a superficial layer of material. Progression of the active site toward the mouth stops after about 30 h. Dissolution then localizes at a critical distance from the mouth, being controlled, autonomously, by the diffusion conditions near the crevice mouth, where dilute electrolyte enforces conditions that are well-approximated by the boundary condition we imposed in the model at that end (see Fig. 9). This relative spatial stagnation of the active site leads to deep carving into the washer near the crevice mouth. This observation is consistent with other studies on crevice corrosion in Nickel alloy 625 washers [67–69]. It is interesting to observe that the model also correctly captures the higher slope of the left wall of the deep trench compared to that of the right wall, which is easily observed in the experimental results reproduced in Fig. 10 (see bottom three figures). The reason for this particular feature can be easily understood when watching the movie in Supplementary Materials: even after localization of the active site, a slow drift to the left (towards the crevice mouth) is still present, which leaves behind the less abrupt (lower-slope) right trench wall.

The PD model presented here helps us explain the underlying mechanism in crevice corrosion. According to the simulation results, the accumulated ions at the closed end locally increase the current density, which produces more dissolved metal ions; the closed end quickly saturates locally, due to the slow diffusion rate along the almost one-dimensional (narrow and long) path towards the crevice mouth; the current density peak starts to travel to towards the mouth, along with the location in the electrolyte between the saturated and the dilute regions, where the concentration is high enough (to cause a large current) to lead to dissolution but smaller than C_{sat}; as the solution saturates, the solid does not passivate but saturation induces diffusion controlled corrosion with a significantly lower diffusion/dissolution rate; corrosion damage slows down in the vertical direction, into the washer; as the current peak location keeps moving towards the mouth, it reaches a location at a critical distance from the mouth where the diffusion rate is high enough to prevent further saturation (as the shorter distance to the dilute electrolyte results in a higher diffusion flux), and the dissolution and diffusion rates become balanced; when this process reaches semi-steady state transport, the peak current density location with high $C < C_{\text{sat}}$ slows its translation to the left, it somewhat stabilizes, causing a deep attack in that particular region. Note that all this complex behavior is obtained autonomously by the PD model that only uses a simple concentration-dependent k_{diss}. The PD crevice corrosion model introduced here is the first computational model to validate experimental results on crevice corrosion damage evolution with such a high level of details.

As seen from the results in Fig. 10, the deep trenches carved in the crevice corrosion process can serve as initiation points for cracks in SCC. Given its ability to simulate fracture in all its complexity [36,52], peridynamics is uniquely positioned to simulate SCC by simply coupling the PD corrosion damage model to a PD fracture model as done in, for example, [38], where pit-to-crack transition in a turbine steel was accurately predicted.

We note that the model introduced here is not only capable of qualitatively matching experimental results, but also quantitatively. As seen from Fig. 10, the evolution of the corrosion damage front and the depth of the local attack found by the PD model are very similar to those from experiments. Please note that the panels with the experimental data are showing the corrosion front for different washers used in distinct tests. Some small differences between the simulation results and the experiments are in terms of surface roughness at the main damage site. This can be attributed to the boundary condition imposed in the model ($C = 0$ is set at a crevice mouth), which is not going to be exactly satisfied in the experiment, due to convection, etc. Moreover, the presence of microstructural heterogeneities in the metal were not considered in the current PD model may also play a role. These, however, could be added by using explicit representation of grain and grain boundaries (e.g. [32]). To reduce the likely high computational cost of such a model, an alternative would be to incorporate microstructural influences using the ideas from the *intermediate homogenization (IH)* PD modeling [70,71]. Another small difference between the simulation and the experiment is the location of the deep attack (critical distance). Note that the experiments in [42], in addition to the variability between different washers used in distinct tests, show a considerable degree of variability for this critical distance along *different radial directions* of the *same* washer in the same experiment (see Figure. 70 in [42]). There are several reasons for this variability, including imperfections in the shape of the washers, the pressure between them, slight asymmetries, etc. On the other hand, the model used here has many simplifications and assumptions, including using a two-dimensional approximation for simulating the actual 3D crevice problem. While a 3D PD simulation can be attempted, an axisymmetric PD corrosion formulation could offer results similar to those of a 3D simulation at a fraction of the cost. This is planned for the future.

As noted earlier, one can study the influence of various environmental conditions on the damage profile by choosing the appropriate functions that describe the corrosion rate as a function of C. In this study, $i(C)$ depended on two functions: 1) $i(\text{pH})$ taken from polarization curves, and 2) $\text{pH}(C)$ obtained from electrochemical relationships. Because of these dependencies, having a different concentration of chloride in the bulk, for example, changes the function $\text{pH}(C)$ (see [26]), which, in turn, changes the $i(C)$ function. Since damage evolution is driven by this function, we can study the influence of the bulk concentration of chloride on the damage evolution/profile. A detailed study of these effects is, however, left for the future.

6. Conclusions

A new peridynamic (PD) model for crevice corrosion damage was introduced and validated against experimental results from the published literature. We reduced the self-accelerating anodic dissolution kinetics in crevice corrosion to a metal-ion concentration-dependent current density relationship. This rela-

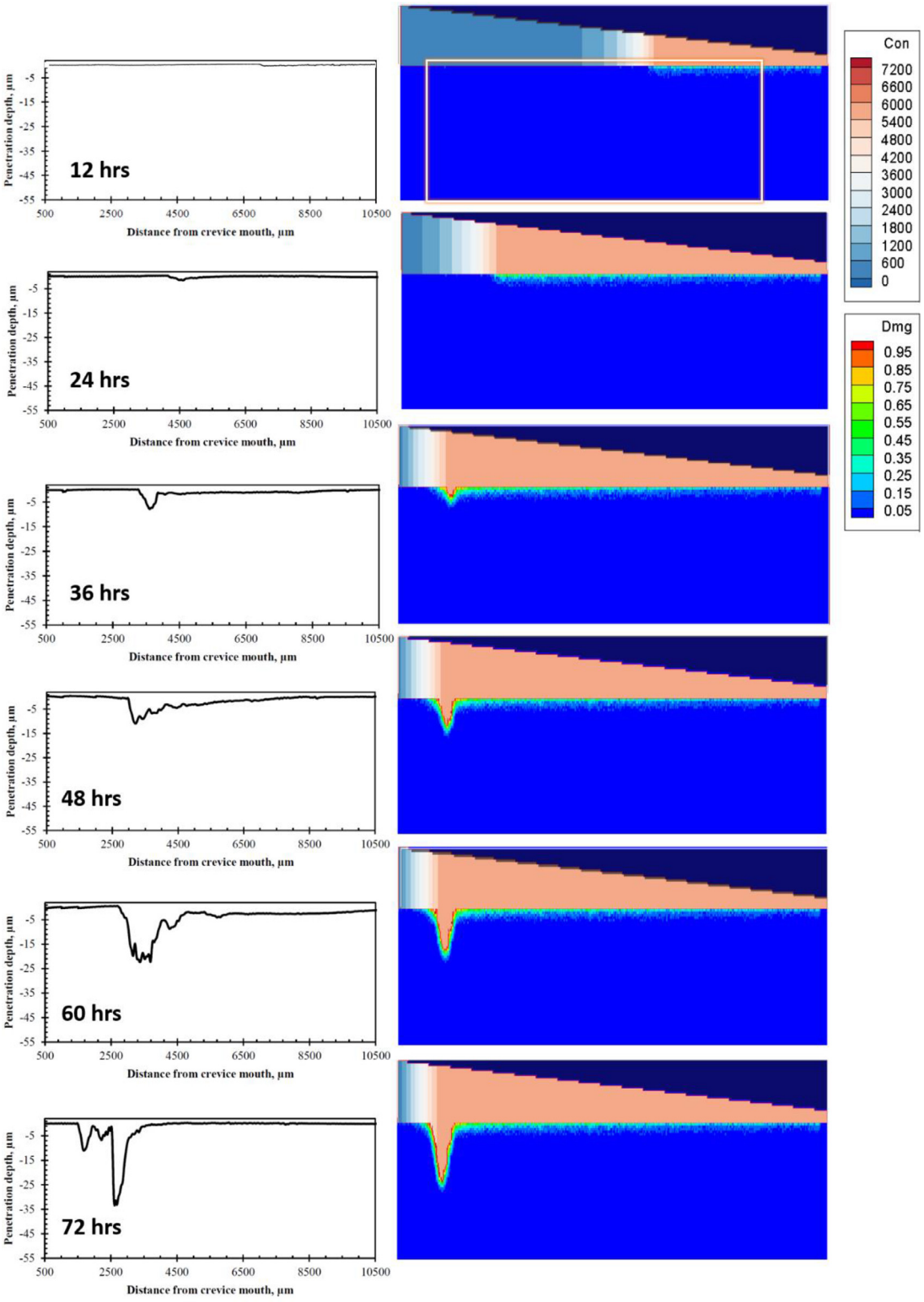

Fig. 10. Comparison of experimental results (left column, from [42]; note that each panel is from distinct washers coming from distinct experiments) and PD simulation results for crevice corrosion. The time and length scales for simulation and experiments are identical. The colors in the metal region (see Fig. 9) show the evolution of the nodal damage index, while those in the electrolyte region (see Fig. 9) indicate the metal ion concentration in the crevice.

tionship defines the local micro-dissolvability for interfacial PD transport bonds that carry anodic dissolution micro-fluxes. To be able to compute efficiently problems defined over domains with extreme aspect ratios, discretizations with similar aspect ratios are desired, but they were not possible in the standard PD formulation. To solve this problem, we presented a generalized version of the PD formulation that allows horizons with arbitrary shapes. In turn, discretizations with highly different grid spacings in different directions are now possible. This plays a crucial role in efficiently simulating crevice corrosion, since crevices are often long

but very narrow (with differences of two-three orders of magnitude between their effective length and gap). The model was validated against an experiment from literature on crevice corrosion between two washers of nickel alloy 625. We found the concentration-dependent current density from experimental polarization curves and analytical/empirical relationships. A PD model with the simple concentration-dependent dissolution formulation is able to predict the kinetics of anodic dissolution and damage evolution inside the crevice in great detail. This also demonstrates that it is sufficient to consider the two factors: concentration-dependent dissolution, and diffusion-driven transport of dissolved metal ions, to explain the evolution of crevice corrosion.

Author contributions

Siavash Jafarzadeh: Methodology, Investigation, Software, Writing- Original draft, Validation, Writing-Review and Editing, Visualization. **Jiangming Zhao**: Software, Writing- Reviewing and Editing. **Mahmoud Shakouri**: Methodology, Writing- Reviewing and Editing. **Florin Bobaru:** Conceptualization, Methodology, Writing- Reviewing and Editing, Supervision, Project Administration, Funding Acquisition.

Declaration of Competing Interest

The authors declare that they have no known competing financial interests or personal relationships that could have appeared to influence the work reported in this paper.

Acknowledgements

The authors express their gratitude to the anonymous reviewers whose pertinent questions and comments led to a much improved version of the manuscript. The work of S.J., J.Z. and F.B. was supported by the National Science Foundation under CMMI award No. 1953346, and by a Nebraska System Science award from the Nebraska Research Initiative. The computations have been performed utilizing the Holland Computing Center of the University of Nebraska, which receives support from the Nebraska Research Initiative.

Supplementary materials

Supplementary material associated with this article can be found, in the online version, at doi:10.1016/j.electacta.2021.139512.

References

[1] P. Marcus, Corrosion Mechanisms in Theory and Practice, CRC Press, 2011.
[2] E. McCafferty, Introduction to Corrosion Science, Springer Science & Business Media, 2010.
[3] A. Betts, L. Boulton, Crevice corrosion: review of mechanisms, modelling, and mitigation, Br. Corros. J. 28 (1993) 279–296.
[4] D. Johns, K. Shemwell, The crevice corrosion and stress corrosion cracking resistance of austenitic and duplex stainless steel fasteners, Corros. Sci. 39 (1997) 473–481.
[5] S.-.K. Lee, J. Zielske, An FHWA special study: post-tensioning tendon grout chloride thresholds, National Transportation Library, U.S. Department of Transportation, Federal Highway Administration, 2014.
[6] S. Jafarzadeh, Z. Chen, F. Bobaru, Computational modeling of pitting corrosion, Corros. Rev. 37 (2019) 419–439.
[7] J.W. Fu, S.-K. Chan, A finite element method for modeling localized corrosion cells, Corrosion 40 (1984) 540–544.
[8] S. Sharland, C. Jackson, A. Diver, A finite-element model of the propagation of corrosion crevices and pits, Corros. Sci. 29 (1989) 1149–1166.
[9] M. Watson, J. Postlethwaite, Numerical simulation of crevice corrosion: the effect of the crevice gap profile, Corros. Sci. 32 (1991) 1253–1262.
[10] Y. Xu, H.W. Pickering, The initial potential and current distributions of the crevice corrosion process, J. Electrochem. Soc. 140 (1993) 658.
[11] J. Walton, G. Cragnolino, S. Kalandros, A numerical model of crevice corrosion for passive and active metals, Corros. Sci. 38 (1996) 1–18.
[12] H.-.Y. Chang, Y.-.S. Park, W.-.S. Hwang, Initiation modeling of crevice corrosion in 316 L stainless steels, J. Mater. Process. Technol. 103 (2000) 206–217.
[13] K. Heppner, R. Evitts, J. Postlethwaite, Effect of the crevice gap on the initiation of crevice corrosion in passive metals, Corrosion 60 (2004) 718–728.
[14] J. Lee, M. Reed, R. Kelly, Combining rigorously controlled crevice geometry and computational modeling for study of crevice corrosion scaling factors, J. Electrochem. Soc. 151 (2004) B423–B433.
[15] G.F. Kennell, R.W. Evitts, K.L. Heppner, A critical crevice solution and IR drop crevice corrosion model, Corros. Sci. 50 (2008) 1716–1725.
[16] X. Chen, F. Gao, Y. Wang, C. He, Transient numerical model for crevice corrosion of pipelines under disbonded coating with cathodic protection, Mater. Des. 89 (2016) 196–204.
[17] W. Wang, K. Shen, J. Yi, Q. Wang, A mathematical model of crevice corrosion for buried pipeline with disbonded coatings under cathodic protection, J. Loss Prev. Process. Ind. 41 (2016) 270–281.
[18] C. Cui, A. Chen, Z. Pan, R. Ma, Two-dimensional numerical model and fast estimation method for calculating crevice corrosion of cross-sea bridges, Constr. Build. Mater. 206 (2019) 683–693.
[19] M. Tachibana, Y. Wada, T. Arakawa, Y. Kikuchi, T. Seto, Development of the fundamental multiphysics analysis model for crevice corrosion using a finite element method, in: Proceedings of the 18th International Conference on Environmental Degradation of Materials in Nuclear Power Systems–Water Reactors, Springer, 2019, pp. 1713–1723.
[20] Y. Onishi, J. Takiyasu, K. Amaya, H. Yakuwa, K. Hayabusa, Numerical method for time-dependent localized corrosion analysis with moving boundaries by combining the finite volume method and voxel method, Corros. Sci. 63 (2012) 210–224.
[21] W. Sun, L. Wang, T. Wu, G. Liu, An arbitrary Lagrangian–Eulerian model for modelling the time-dependent evolution of crevice corrosion, Corros. Sci. 78 (2014) 233–243.
[22] R. Duddu, N. Kota, S.M. Qidwai, An extended finite element method based approach for modeling crevice and pitting corrosion, J. Appl. Mech. 83 (2016) 081003.
[23] Z. Xiao, S. Hu, J. Luo, S. Shi, C. Henager Jr, A quantitative phase-field model for crevice corrosion, Comput. Mater. Sci. 149 (2018) 37–48.
[24] J. Ding, H. Wang, E.-.H. Han, A multiphysics model for studying transient crevice corrosion of stainless steel, J. Mater. Sci. Technol. 60 (2021) 186–196.
[25] M.D. Brackman, C. Clemons, D. Golovaty, K. Kreider, J. Wilder, G. Young, J. Payer, R. Lillard, Modeling and simulation of damage evolution during crevice corrosion, J. Electrochem. Soc. 161 (2014) C237–C245.
[26] A. Stenta, C. Clemons, D. Golovaty, K. Kreider, G. Young, D. Salgado, S. Lillard, Species-dependent crevice corrosion modeling of Ni-625, Corrosion 72 (2016) 1328–1341.
[27] J. Zhao, S. Jafarzadeh, M. Rahmani, Z. Chen, Y.-.R. Kim, F. Bobaru, A peridynamic model for galvanic corrosion and fracture, Electrochim. Acta 391 (2021) 138968.
[28] D. Di Caprio, C. Vautrin-Ul, J. Stafiej, J. Saunier, A. Chaussé, D. Féron, J. Badiali, Morphology of corroded surfaces: contribution of cellular automaton modelling, Corros. Sci. 53 (2011) 418–425.
[29] C. Cui, R. Ma, A. Chen, Z. Pan, H. Tian, Experimental study and 3D cellular automata simulation of corrosion pits on Q345 steel surface under salt-spray environment, Corros. Sci. 154 (2019) 80–89.
[30] Z. Chen, F. Bobaru, Peridynamic modeling of pitting corrosion damage, J. Mech. Phys. Solids 78 (2015) 352–381.
[31] S. Jafarzadeh, Z. Chen, F. Bobaru, Peridynamic modeling of repassivation in pitting corrosion of stainless steel, Corrosion 74 (2018) 393–414.
[32] S. Jafarzadeh, Z. Chen, F. Bobaru, Peridynamic modeling of intergranular corrosion damage, J. Electrochem. Soc. 165 (2018) C362–C374.
[33] S. Jafarzadeh, Z. Chen, J. Zhao, F. Bobaru, Pitting, lacy covers, and pit merger in stainless steel: 3D peridynamic models, Corros. Sci. 150 (2019) 17–31.
[34] J. Mehrmashhadi, M. Bahadori, F. Bobaru, On validating peridynamic models and a phase-field model for dynamic brittle fracture in glass, Eng. Fract. Mech. 240 (2020) 107355.
[35] F. Mousavi, S. Jafarzadeh, F. Bobaru, An ordinary state-based peridynamic elastoplastic 2D model consistent with J2 plasticity, Int. J. Solids Struct. (2021) 111146.
[36] J. Zhao, Z. Chen, J. Mehrmashhadi, F. Bobaru, A stochastic multiscale peridynamic model for corrosion-induced fracture in reinforced concrete, Eng. Fract. Mech. 229 (2020) 106969.
[37] S. Jafarzadeh, Z. Chen, S. Li, F. Bobaru, A peridynamic mechano-chemical damage model for stress-assisted corrosion, Electrochim. Acta 323 (2019) 134795.
[38] Z. Chen, S. Jafarzadeh, J. Zhao, F. Bobaru, A coupled mechano-chemical peridynamic model for pit-to-crack transition in stress-corrosion cracking, J. Mech. Phys. Solids 146 (2021) 104203.
[39] W. Mai, S. Soghrati, R.G. Buchheit, A phase field model for simulating the pitting corrosion, Corros. Sci. 110 (2016) 157–166.
[40] W. Mai, S. Soghrati, A phase field model for simulating the stress corrosion cracking initiated from pits, Corros. Sci. 125 (2017) 87–98.
[41] C. Cui, R. Ma, E. Martínez-Pañeda, A phase field formulation for dissolution–driven stress corrosion cracking, J. Mech. Phys. Solids 147 (2021) 104254.
[42] D.R. Muñoz Salgado, Crevice corrosion in Nickel Alloy 625 in an ocean water environment, Chemical Engineering, University of Akron, 2017.
[43] S.A. Silling, R.B. Lehoucq, Peridynamic theory of solid mechanics, Adv. Appl. Mech. 44 (2010) 73–168.
[44] F. Bobaru, J.T. Foster, P.H. Geubelle, S.A. Silling, Handbook of Peridynamic Modeling, CRC Press, 2016.

[45] Z. Chen, G. Zhang, F. Bobaru, The influence of passive film damage on pitting corrosion, J. Electrochem. Soc. 163 (2016) C19–C24.
[46] S. Li, Z. Chen, F. Wang, B. Cui, L. Tan, F. Bobaru, Analysis of corrosion-induced diffusion layer in ZK60A magnesium alloy, J. Electrochem. Soc. 163 (2016) C784–C790.
[47] N. Badwe, X. Chen, D.K. Schreiber, M.J. Olszta, N.R. Overman, E. Karasz, A. Tse, S.M. Bruemmer, K. Sieradzki, Decoupling the role of stress and corrosion in the intergranular cracking of noble-metal alloys, Nat. Mater. 17 (2018) 887–893.
[48] S. Li, Z. Chen, L. Tan, F. Bobaru, Corrosion-induced embrittlement in ZK60A Mg alloy, Mater. Sci. Eng. 713 (2018) 7–17.
[49] R. Vallabhaneni, T.J. Stannard, C.S. Kaira, N. Chawla, 3D X-ray microtomography and mechanical characterization of corrosion-induced damage in 7075 aluminium (Al) alloys, Corros. Sci. 139 (2018) 97–113.
[50] D. Yavas, P. Mishra, A. Alshehri, P. Shrotriya, K.R. Hebert, A.F. Bastawros, Nanoindentation study of corrosion-induced grain boundary degradation in a pipeline steel, Electrochem. Commun. 88 (2018) 88–92.
[51] S.A. Silling, E. Askari, A meshfree method based on the peridynamic model of solid mechanics, Comput. Struct. 83 (2005) 1526–1535.
[52] F. Bobaru, G. Zhang, Why do cracks branch? A peridynamic investigation of dynamic brittle fracture, Int. J. Fract. 196 (2015) 59–98.
[53] U.M. Ascher, C. Greif, A First Course on Numerical Methods, SIAM, 2011.
[54] N. Laycock, J. Stewart, R. Newman, The initiation of crevice corrosion in stainless steels, Corros. Sci. 39 (1997) 1791–1809.
[55] J. De Gruyter, S. Mertens, E. Temmerman, Corrosion due to differential aeration reconsidered, J. Electroanal. Chem. 506 (2001) 61–63.
[56] B. Kehler, J. Scully, Role of metastable pitting in crevices on crevice corrosion stabilization in alloys 625 and 22, Corrosion 61 (2005) 665–684.
[57] N. Laycock, R. Newman, Localised dissolution kinetics, salt films and pitting potentials, Corros. Sci. 39 (1997) 1771–1790.
[58] Z. Chen, F. Bobaru, Selecting the kernel in a peridynamic formulation: a study for transient heat diffusion, Comput. Phys. Commun. 197 (2015) 51–60.
[59] F. Bobaru, W. Hu, The meaning, selection, and use of the peridynamic horizon and its relation to crack branching in brittle materials, Int. J. Fract. 176 (2012) 215–222.
[60] F. Bobaru, M. Duangpanya, A peridynamic formulation for transient heat conduction in bodies with evolving discontinuities, J. Comput. Phys. 231 (2012) 2764–2785.
[61] A. Ahadi, J. Krochmal, Anisotropic peridynamic model—Formulation and implementation, AIMS Mater. Sci. 5 (2018) 742–755.
[62] T. Mei, J. Zhao, Z. Liu, X. Peng, Z. Chen, F. Bobaru, The role of boundary conditions on convergence properties of peridynamic model for transient heat transfer, J. Sci. Comput. 87 (2021) 50.
[63] R. Lillard, M. Jurinski, J. Scully, Crevice corrosion of alloy 625 in chlorinated ASTM artificial ocean water, Corrosion 50 (1994).
[64] Q. Le, F. Bobaru, Surface corrections for peridynamic models in elasticity and fracture, Comput. Mech. 61 (2018) 499–518.
[65] J. Zhao, S. Jafarzadeh, Z. Chen, F. Bobaru, An algorithm for imposing local boundary conditions in peridynamic models on arbitrary domains, engrXiv Preprints (2020), doi:10.31224/osf.io/7z8qr.
[66] J.R. Shewchuk, Department of Computer Science, Carnegie-Mellon University, 1994.
[67] R. Lillard, S. Mehrazi, D. Miller, Quantifying Alloy 625 crevice corrosion using an image differencing technique: part i. initiation and propagation, J. Electrochem. Soc. 167 (2020) 021511.
[68] R. Lillard, D. Miller, C. Clemons, K. Kreider, G. Young, Quantifying Alloy 625 crevice corrosion using an image differencing technique: part II. a diffusive transport model of crevice cation concentration using surface current density, J. Electrochem. Soc. 167 (2020) 141503.
[69] R. Lillard, S. Mehrazi, Quantifying Alloy 625 crevice corrosion using an image differencing technique: part iii. the transition from diffusion to activation control and the implications for the measured electrochemical potentials, J. Electrochem. Soc. 168 (2021) 021511.
[70] J. Mehrmashhadi, Z. Chen, J. Zhao, F. Bobaru, A stochastically homogenized peridynamic model for intraply fracture in fiber-reinforced composites, Compos. Sci. Technol. 182 (2019) 107770.
[71] P. Wu, J. Zhao, Z. Chen, F. Bobaru, Validation of a stochastically homogenized peridynamic model for quasi-static fracture in concrete, Eng. Fract. Mech. 237 (2020) 107293.